Biosensors and Bioelectronics 169 (2020) 112546

Contents lists available at ScienceDirect

Biosensors and Bioelectronics

journal homepage: http://www.elsevier.com/locate/bios

TFT sensor array for real-time cellular characterization, stimulation, impedance measurement and optical imaging of *in-vitro* neural cells

Faruk Azam Shaik [a,b,*], Satoshi Ihida [a,c], Yoshiho Ikeuchi [a], Agnès Tixier-Mita [a], Hiroshi Toshiyoshi [a]

[a] Institute of Industrial Science, The University of Tokyo, 4-6-1 Komaba, Meguro, Tokyo, 153-8505, Japan
[b] UMR 8161, Faculty of Medicine, University of Lille, France
[c] Sharp Corporation, 1-2-3 Shibaura, Minato, Tokyo, 105-0023, Japan

ARTICLE INFO

Keywords:
Thin film transistor
Microelectrode array
Biosensor
Impedance spectroscopy
Extracellular recording

ABSTRACT

Real-time *in-vitro* multi-modality characterization of neuronal cell ensemble involves highly complex interdependent phenomena and processes. Although a variety of microelectrode arrays (MEAs) have been reported, diagnosis techniques are limited in term of sensing area, optical transparency, resolution and number of modalities. This paper presents an optically transparent thin-film-transistor (TFT) array biosensor chip for neuronal ensemble investigation, in which TFT electrodes are used for six modalities including extracellular voltage recording of both action potential (AP) and local field potential (LFP), current or voltage stimulation, chemical stimulation, electrical impedance measurement, and optical imaging. The sensor incorporates a large sensing area (15.6 mm × 15.6 mm) with a 200 × 150 array of indium-tin-oxide (ITO) electrodes placed at a 50 μm or 100 μm pixel pitch and with 10 ms temporal resolution; these performances are comparable to the state-of-the-art MEA devices. The TFT electrode array is designed based on the switch matrix architecture. The reliability and stability of TFTs are examined by measuring their electrical characteristics. Impedance spectroscopy function is verified by mapping the neuron position and the status (cells alive or dead, contamination) on the electrodes, which facilitates the biochemical studies in electrical domain that adds quantitative views to visual observation of cells through the optical microscopy. An *in-vitro* neuron culture is studied using electrophysiological, electrochemical, and optical characterization. Detailed signal analysis is demonstrated to prove the capability of bioassay.

1. Introduction

Demands for investigating the neuronal networks and the functions of the nervous system are escalating in the field of advanced *in-vitro* drug screening (Park et al., 2015) to cope with the central nervous system diseases such as neurodevelopmental, psychiatric, and neurodegenerative disorders (Grskovic et al., 2011). The electrogenic cells generating electrical signals facilitate the study in the electrical domain under *in-vitro* or *in-vivo* conditions (Azim et al., 2019; Cohen-Karni et al., 2010; Hess et al., 2011; Santoro et al., 2014; Shaik et al., 2020). The *in-vivo* study of complex neuronal networks is challenging because of the physiological complications, ethical dilemmas, and additional filtration. *In-vitro* neuronal study, being further classified as either extracellular or intracellular, uses measurement tools such as patch-clamp and sharp microneedle probes. Although intracellular study has an advantage of a high signal-to-noise ratio (Angle et al., 2015), it has several major drawbacks such as mechanical instability, incompatibility with multisite recording, and a risk of fluid contamination or dilution with the electrode fluid in the case of patch-clamp studies, all of these resulting in inaccurate diagnosis (Pottosin and Dobrovinskaya, 2015). Understanding the brain functions, for instance, depends mostly on the extracellular recording, which consists of direct measurement of electrical activities from recording electrodes placed close to the neuronal cell culture without causing damage to the neuron's plasma membrane (Aziz et al., 2009; Kim et al., 2015; Ruther and Paul, 2015; Shen et al., 2015). The resulting voltage signals are composed of the local field potentials (LFPs) and the spikes emitted by one or more neurons (Zanos et al., 2011).

To develop an *in-vitro* model through the study of neural dynamics, an ideal readout device needs to have the following features: biocompatibility, optical transparency (for fluoroscopy analyses), high fill

* Corresponding author. Institute of Industrial Science, The University of Tokyo, 4-6-1 Komaba, Meguro, Tokyo, 153-8505, Japan.
E-mail addresses: faruk@iis.u-tokyo.ac.jp, faruk-azam.shaik@univ-lille.fr (F.A. Shaik).

https://doi.org/10.1016/j.bios.2020.112546
Received 9 June 2020; Received in revised form 20 August 2020; Accepted 22 August 2020
Available online 30 August 2020

factor, large sensor area, on-chip multiplexing, bidirectional interface, fast temporal response, and high spatial resolution. Traditional multi-electrode-array (MEA) devices are electrically passive and planar in shape with metal electrodes on top of a glass substrate (Abdelfattah et al., 2016; Foidl et al., 2018; Franke et al., 2017). However, due to the congestion problem of electrical interconnection, MEAs usually have limited number of independent electrodes, resulting in a low density and a low throughput of measurement (Cabello et al., 2018; Hood et al., 2009; Lu et al., 2016; Spira and Hai, 2013). On the contrary, complementary metal-oxide semiconductor (CMOS) arrays can accommodate a large number of electrodes at a high density. Nonetheless, silicon substrate for CMOS technology is opaque, and it would not allow visual observation by the inverted microscope (Bertotti et al., 2014; Cabello et al., 2018; Heer et al., 2006; Park et al., 2018; Snell et al., 1981).

Besides MEA and CMOS technologies, thin film transistor (TFT) technology is expected to play an increasing role for the electrophysiology. TFT is a well-known technology for flat panel display (Snell et al., 1981). Several milestones have been attained (Brody et al., 1973; Le Comber et al., 1979; Spear and Le Comber, 1993; Yamamoto, 2012) since the first TFTs were made of a compound semiconductor called cadmium sulfide (CdS), which was introduced in 1962 by Weimer (1962). Hosono's group with the Tokyo Institute of Technology, Japan, first explored the semiconducting indium gallium zinc oxide (IGZO) as a TFT channel material, and demonstrated crystalline and amorphous IGZO-TFTs in 2003 and 2004, respectively (Nomura et al., 2004, 2003).

In this paper, we present a transparent high-definition crystalline-IGZO-TFT system as a bio-measurement platform. The device chip is made by the same fabrication technology for the liquid-crystal display (LCD) fabrication. The crystalline-IGZO is an optically transparent semiconductor material with electron mobility of 20–50 times higher than that of amorphous silicon. In this study, crystalline-IGZO-TFTs are used as a transparent substrate for see-through observation of bio-tissue, and the high electron mobility is adopted for high-speed recording of the ionic behaviors. The system based on the TFT technology thus benefits from the optical transparency and high-density electronics to produce a sensor array of various cell analysis.

The purpose of this paper is to demonstrate all the potentials of TFT systems applicable to a neuron culture. Previous reports from the authors' group demonstrated a singular modality (neuron sensing only, or impedance sensing). The different aspects of the systems are described in the following sections. The system architecture, corresponding functional units, and their integration are described in Sections 2. The electrical characterization and measurements as well as the biological measurements are described in Section 3. Sections 4 and 5 respectively give a detailed summary and comparison to the states-of-the-art measurement methods.

2. Methods

2.1. System architecture

Crystalline-IGZO-TFT in this work is designed to perform multiple stimulation/measurement functions as schematically shown in Fig. 1(a) by appropriately choosing the electrode sites (Shaik et al., 2018, 2017). The block diagram in Fig. 1(b) illustrates the system architecture, where all the functional units are depicted. Typical chip has 175 × 175 TFT microelectrodes over an area of 243 mm^2. TFTs plates of several cm^2 or more are achievable, which is useful for organ-on-chip study (Wikswo et al., 2013) and to overcome the complex processes of drug development (Dietzel, 2016). The optical transparency of substrate is also beneficial to optogenetic studies (Lee et al., 2015). In addition to optical studies, two more sensing techniques are used thanks to the presence of high density of microelectrodes: 2D action potential mapping for neurons network activity, and 2D impedance spectroscopy for the neurons culture. Impedance spectroscopy can give various information on the neurons including the status of presence or absence, alive or dead, infection, detachment, and best recording area with the culture neurons. Detail of each functional unit is discussed later.

2.2. Electrode array

TFTs are one of field-effect transistors (FETs), with the advantage of large area, substrate versatility, and low temperature fabrication, while costly high-temperature processes are used for metal oxide semiconductor field-effect transistors (MOSFET) (Correia et al., 2016). Both TFTs and MOSFETs use three parts (gate, source, and drain) made of electrically conductive, semi-conductive, and dielectric materials. The semi-conducting layer is located in between the conductive source and drain, whereas the dielectric is placed between the conductive gate and the semiconducting channel layer. They are also sorted out by the position of the gate on either top or bottom with respect to the channel layer (Correia et al., 2016). The TFTs device in this work is a bottom-gate coplanar type.

The electrode array was fabricated on a 27 mm × 25 mm glass substrate and was composed of 30,000 electrodes placed at a pitch of 50–100 μm for 200 × 150 pixels, covering an area of 243 mm^2. A

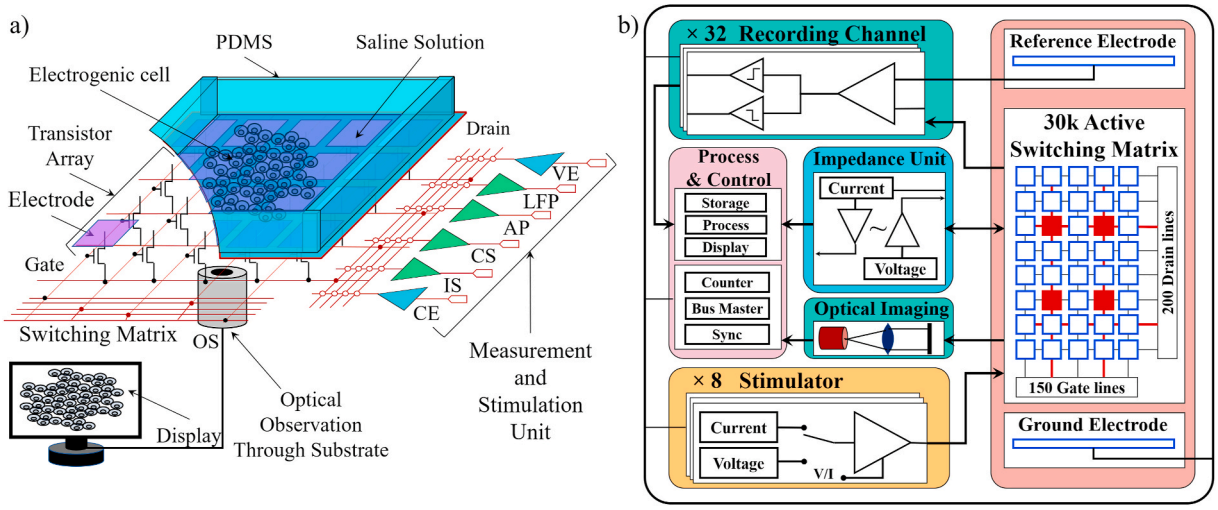

Fig. 1. a) Schematic illustration of the functions of switch matrix based on thin film transistor (TFT) system featuring current excitation (CE), impedance measurement (IM), current sensing (CS), action potential (AP) sensing, local field potential (LPF) sensing, voltage excitation (VE), and optical sensing (OS). b) Block diagram of the multimodality TFT system that includes active switching matrix, recording channel, stimulator, impedance spectroscopy unit, and optical imaging.

schematic of a single electrode and circuit is shown in Fig. 2(a). The source of each transistor was connected to an ITO electrode, and accessed through a 2D-addressed transistor. Each transistor had two electrical interconnections called the gate and the drain lines, by which the target electrodes were spatially chosen. The gate line was used to activate the transistor, and the drain line was used for electrical measurement or stimulation. The electrode arrays were made of indium-thin-oxide (ITO), and had direct contact with the transistor source, wherein the gate of the transistor was made of crystalline-IGZO material. The pixel resolution was 359.2 pixels per inch (70.7 μm per pixel), and the temporal response was 10 ms. The electrodes had negligible power consumptions because of the small size, which lead to negligible heating effect, thereby protecting biological cells from death. The electrodes covered 90% of the total active surface area, with a transparency of above 90%, being well suited for both electrical and optical characterization of biological samples. The design of the featured electrodes matched with the dimension of the primary neurons, 10–30 μm in diameter and more than 100 μm in length (Harris, 2018), being capable of performing all the proposed measurements and stimulations.

2.3. System integration

For device development, the TFT substrate was cleaned and attached to a pre-drilled printed circuit board (PCB) for an observation window. A wire of 1% silicon aluminum alloy, with 25 μm in diameter, was used for the electrical connection between the PCB and the TFT by a wire-bonder operated at 0.396 W ultrasonic power and 30 N bonding force (TABN-25H25, TANAKA). A Polydimethylsiloxane (PDMS) chamber was prepared by the standard processes (Park et al., 2006), which included a 1:10 mixture of curing agent and PDMS monomer; after the air bubbles were removed by vacuuming, the polymer was solidified by heat treatment at 90 °C for 30 min. An 8-mm-high PDMS chamber was formed with the inner and the outer diameters of 6 mm and 8 mm, respectively. The PDMS chamber was pressure-bonded onto the TFT plate. Extra care was taken to protect the bonded wires from damaging when fixing them with additional molten PDMS to mold. The TFT electrodes were accessed using the 28 pins on the PCB. Data bus and address bus between the PCB and the measurement/stimulation units were made by using universal serial bus cables, push/pull connectors, synchronized connectors, and

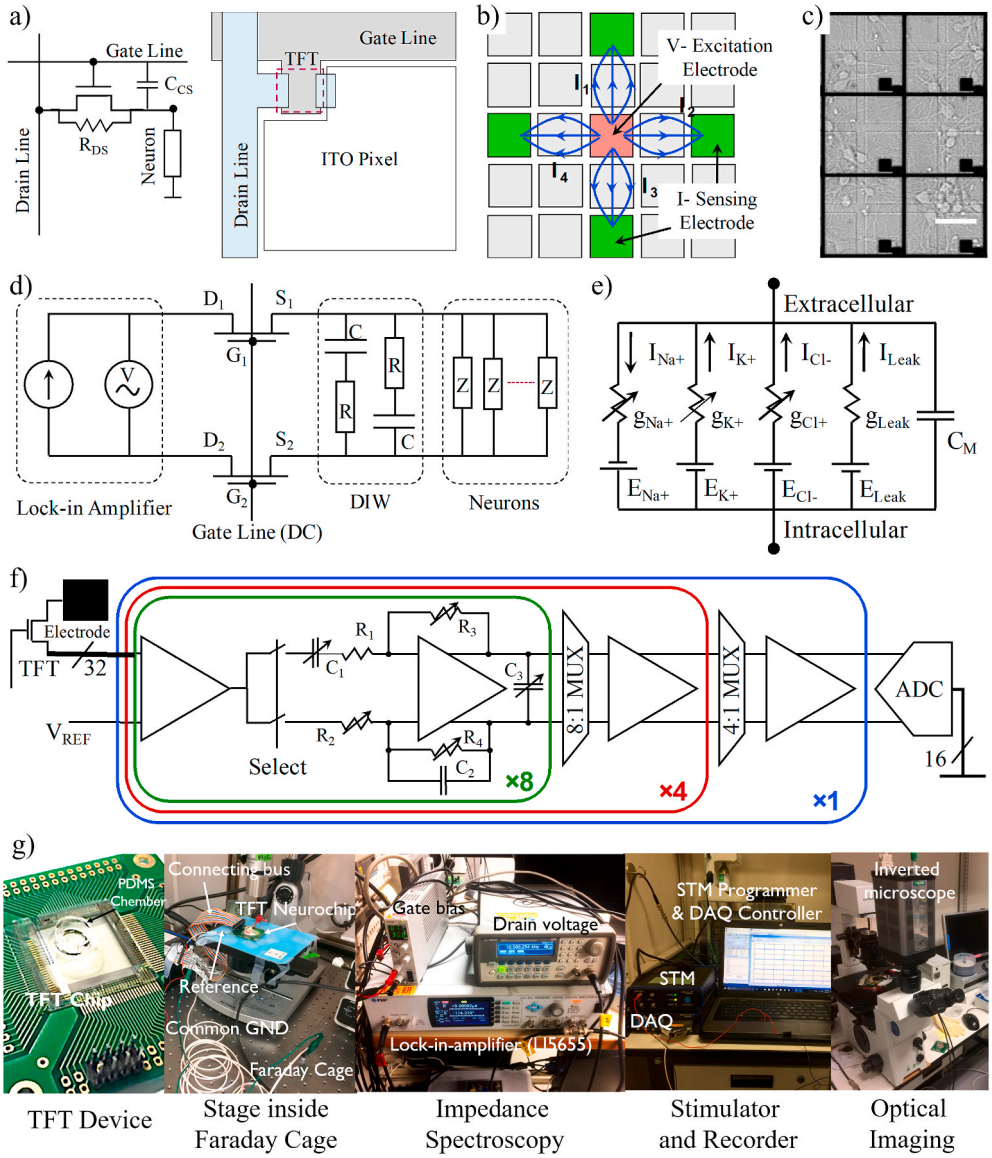

Fig. 2. Overall system. (a) Schematic diagram of an arrayed pixel and electrical switching system. (b) Cellular impedance measured by voltage excitation and current sensing. (c) Neuron culture on top of the array. (d) Circuit diagram of impedance measurement. (e) Equivalent circuit model for the basic neuron. (f) Schematic of recording system. (g) Experimental assembly of instruments used in this study. Scale bar: (c) 50 μm.

BNC connectors. The measurement was conducted inside the Faraday cages to decouple the environmental electromagnetic interferences.

2.4. Impedance measurement

Electrical impedance Z is an AC analogue of resistance that obeys a variant of Ohm's law, which is expressed by $Z = V/I$, where V and I are the complex forms of voltage and current, respectively. It can be broken down into independently measurable components, i.e. magnitude and phase, as $Z = |V|/|I|e^{j(\omega t-\phi)}$, where ω and ϕ are the frequency and the phase lag, respectively, and $|V|/|I|$ is the magnitude of the overall impedance.

The aim of the impedance measurement in this work is to tell the presence or absence of neuron cells in a given region, by which an appropriate recording electrodes are chosen for further measurement. This method primarily helps to identify a high-density neuron culture region, which is then confirmed by microscopic images. The extracellular potential of a single neuron is measurable within a few tens of micron distance from the soma (Müller et al., 2015), and hence identifying the recording region is crucial to avoid crosstalk of measurement. An AC signal is applied to one of the electrodes, while another proximity electrode is used to read out the output current as shown in Fig. 2(b). This recording process is repeated for different electrodes in a given region, while the input electrode is fixed. When N electrodes are scanned in a given region, the resulting average impedance of the region is written as

$$Z_{\text{region}} = \frac{\sum Z_n}{N},\ Z_n = \frac{V}{I_n} \quad (n = 1,\ 2, \ldots, N). \tag{1}$$

Electrode scan is performed over an area, and the results are superposed over the microscopic images. Due to the neuron presence on the electrode, the real part (resistive) of the impedance decreases with increasing the frequency because the cells behave as a conductive material. The imaginary part (capacitive), on the other hand, tends to increase with increasing the frequency. The increase rate of capacitance is relatively higher than the decrease rate of resistance, resulting in a shift of impedance over the frequency. The impedance characterization not only allows us to find the hot spot in the culture but also tells the state of the cells, such as living/dead in the culture as reported elsewhere (Cathcart et al., 2020, 2017, 2016).

The measurement setup consists of a signal source of 0.05 V_{PP}, which is swept over a range of frequencies. The signal source is applied to the drain of a transistor to avoid the unintentional stimulation, while the gate line is biased to a constant 15 V_{DC} by an Agilent 33,110 signal generator. A synchronous LI5655 lock-in amplifier is connected to an adjacent drain line for current sensing, which is compared with the input voltage signal. Finally, the amplifier convolves the both signals to calculate the magnitude and the phase offset of the current signal with respect to the input voltage signal.

2.5. Electrical stimulator

Stimulation of cells comes after defining the region of study, by using manual switches to choose the signal lines from the TFT plate. The stimulator (STG4000 series from Multi Channel System), which generates waveforms required for specific channels, is used for both current and voltage stimulation. Spatially separated electrodes in the array can be chosen for multi-site stimulation. Proper selection of electrodes is vital to maximize the signal quality (Chu et al., 2017). The drain of the transistor is assigned to the stimulator output, while the corresponding gate of the transistor is electrically biased to a fixed 10 V_{DC}.

2.6. Electrical recording

The data acquisition system (USB-ME32-FAI System from Multi Channel System) of 32 channels is used to continuously scan the voltages for monitoring. A schematic view is illustrated in Fig. 2 (f). A reference electrode of wire Ag/AgCl is kept in the culture bath and maintained at a certain height in the liquid. The system ground is set with a reference electrode that is used to suppress the noise level by ~1/10 times. The MC_Rack software from Multi Channel System is used to display the signal. The gates of all recording transistors are maintained at a constant voltage of 10 V. Sampling rate of 20 kHz is used to extract different extracellular signals such as the AP signals between 300 Hz and 10 kHz and the LFP signals between 1 Hz and 300 Hz. The recording system is equipped with the low- and high-pass filters for sensing the LFPs and the APs, respectively.

2.7. Optical transmissivity

Calcium ions are known for their versatile intracellular signals, which control the fundamental functions of all types of neurons. Calcium imaging in living neurons can directly visualize the intracellular calcium flux in well-defined subcellular compartment (Grienberger and Konnerth, 2012). The platform proposed in this work improves the benchmarking relationship of the patterns of spikes (evoked via both stimulation and spontaneous) with the optically acquired calcium signal, owing to the optical transparency of the substrate and the high electron mobility of IGZO-TFT. In addition, high-speed response of the TFT is advantageous to understand the behavior of spikes/bursting using genetic construction, in which fluorescent proteins would tell the gene expression on a single cell level. In this study, an inverted microscope is used for visual observation through the substrate. The top view observation (for opaque substrate) is inconvenient because of the poor image quality, while observation through a transparent substrate gives better image resolution and more visual information. For usual procedure, we place the TFT plate on the microscope stage, and then the cultured cells of second week are added inside a PDMS microfluidic chamber with Fura-2 dye for fluorescence observation of Ca^{2+} during neurons activity.

2.8. On-chip cell culture

The experiments on animals in this work were performed according to the regulations on laboratory animal welfare of Japan, with the approval of the Center of Biomedical Ethics and Law of The University of Tokyo, Tokyo, Japan.

A 16.5 days pregnant mouse was harvested, and the embryonic were isolated. The standard procedure was used for device preparation and coating, dissection and dissociation (Dunnett and Björklund, 1997). Finally, the TFT plates with 50–300 k cells/device were used to culture the neurons by the standard protocol (Brewer et al., 1993). However, due to rapid evaporation of the culture medium from the small volume of the PDMS chamber, extra medium was added every other day. The nineth-days culture neurons on TFT surface are shown in Fig. 2(c). The equivalent circuit model of the cell is shown in Fig. 2(e), which is represented by an RC band-pass filter bank.

3. Results

3.1. Device characterization

Characterization of the TFT electrodes has been performed to ensure precise and selective stimulation of individual neurons. Typical performances are shown in Fig. 3, including (a) drain voltage response, (b) gate voltage response, (c) frequency response, (d) total harmonic distortion (THD), (e) drain current as a function of transistor gate width, (f) electrolysis test, (g) stress characterization, and (f) optical characterization. The output curves give qualitative information such as the channel pinch-off (saturation) as well as the contact resistance as shown in Fig. 3(a). The transfer curve shown in Fig. 3(b) provides a quantitative analysis for TFTs.

The drain-to-source current (I_{DS}) increases with increasing the gate-

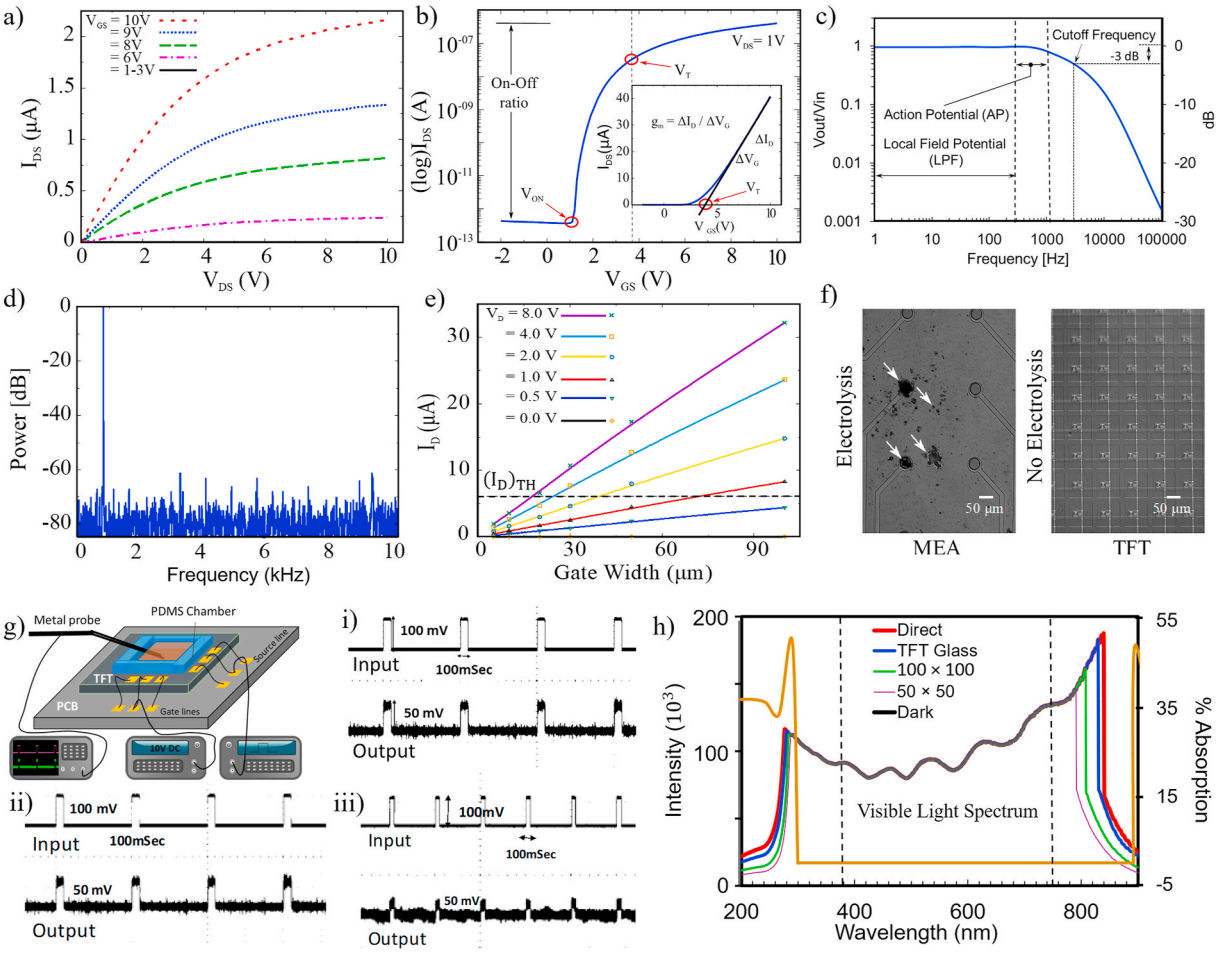

Fig. 3. Typical characteristics of TFT: (a) Drain current, (b) transfer characteristics, (c) frequency response, (d) total harmonic distortion of an array pixel, (e) drain current with respect to gate width, (f) electrolysis test of MEA and TFT, (g) electrochemical testing setup (V_G = 10 V), (i) input through an external metal probe (top) and recording from a drain line (bottom), (ii) input through a drain line (top) and recording from an external metal probe (bottom), (iii) input from drain line (top) and recording from adjacent drain line (bottom), and (h) optical transmission spectrum through the TFT substrate.

to-source voltage (V_{GS}) when applying a positive drain-to-source voltage (V_{DS}). The channel of the transistor is n-type, where electrons are the majority carriers of electrical conductance. The threshold voltage (V_T), at which the current changes significantly due to the gate voltage, is 4 V; the transistor operates in an enhancement mode at gate voltages above 4 V. The turn-on voltage (V_{ON}) is around 1 V, corresponding to V_{GS}, at which the logarithmic I_{DS} curve gives notable change. The figure also allows us to determine the current on/off ratio to be 0.463 × 10^6. The calculated transconductance (g_m) is 0.79 × 10^8 Siemens, which is the ratio of the change in the drain current with respect to the change in the gate voltage. As a result, the field-effect mobility (μ_{FE}) is calculated to be 5 cm^2/Vs. The measured 3 dB cut-off frequency is at around 2 kHz, as shown in Fig. 3(c). To know the total amount of distortion introduced by the TFTs, we have performed spectral analysis to a 1.25 kHz sinusoidal signal as shown in Fig. 3(d); the result exhibits no visible high-order distortion in the frequency spectrum except the fundamental component, thereby indicating the high fidelity monitoring of signals.

The chip has negligible heating effects because of the small dimensions of the transistor compared with the large area to dissipate the heat (4 μm × 4 μm gates over a 100 μm × 100 μm pixel area). The MEA and the TFT have been exposed to the same experimental environment (DC stimulation pulses at 1 kHz for 7 days in a wet environment) and have been reused for a couple of times. We observed electrolysis on the metallic electrodes of the MEA, whereas the TFT was not affected, as shown in Fig. 3(f). The reproducibility and longtime durability of the TFT have been confirmed in the earlier work reported elsewhere (Shaik et al., 2018), wherein more than 1 billion stimulation pulses were applied at 1 kHz for 16 days, both in dry and wet environments, resulting in no electrical leakage.

Current capacity of on-chip stimulation is limited due to the dimension of the transistor, sometimes resulting in insufficient carrier generation. On test electrodes, however, stimulation current could be enhanced by using an appropriate width for the gate, while the length is fixed at 6 μm. The minimum current requirement for stimulation is defined as Rheobase current (Park et al., 2006), which is calculated to be 6.7 μA (Leppert et al., 2016). Judging from the drain current as a function of the gate width shown in Fig. 3(e), a gate width of 17 μm or more would be sufficient for the on-chip current stimulation at V_D = 8 V. The gate width could be further reduced when the drain voltage is increased.

The electrochemical stability of the microelectrodes has been confirmed by stimulation and sensing with a PDMS chamber filled with a culture medium. Three possible combinations of arrangements are used: (i) The signal is applied through an external metal probe and measured from one of the source lines of the transistors, with the gate of the corresponding transistor being pulled up to 10 V. (ii) The signal is supplied from the transistors, and measured by using an external metal probe. (iii) The signal is applied from one of the source lines of the transistors, and the output is measured from the adjacent electrode, with both gates of the corresponding transistors being pulled up to 10 V.

The experimental setup for neuron stimulation and impedance measurement is shown in Fig. 3(g). The input and output signal

waveforms for the different combinations of arrangements are shown in Fig. 3(g) (i-iii): (i) The recorded signal amplitude (50 mV) is found to be half the applied amplitude (100 mV) with a high signal-to-noise (SN) ratio of 80 dB. The recorded signal intensities shown in (i) and (ii) are comparable, thereby implying a possibility of bi-directional signal processing. (iii) The recorded signal amplitude is also found to be half the applied amplitude for the on-chip experiment, which can be used to detect the ionic charges across the cell membrane. The significance of all the three setups is in the compatibility with biological cell experiment in terms of the voltage range of 0–100 mV and the frequency range upwards of 3 kHz.

Optical transparency of the TFT substrate has also been confirmed for the visible spectrum wavelength ranging between 380 nm and 750 nm. A spectrometer (C11119-04, Hamamatsu Photonics) is used to determine the transmission spectra through a sample under test illuminated by a light-emitting diode (LED) of white light spectrum. The spectrometer is initially calibrated in the dark environment only to show the negligible noise level plotted by the black curve in Fig. 3(h), after which the LED at maximum intensity is guided into the spectrometer to determine the source spectrum as plotted by the red curve. A blank glass substrate is inserted in the path to show the spectrum blotted in blue. Finally, the TFT substrates with 100 μm × 100 μm and 50 μm × 50 μm grid electrodes are tested. Compared with the preceding TFT substrate reported elsewhere (Kojiri et al., 2014; Matsuda et al., 2017), which had notable absorption in the visible wavelength range, the latest version of the TFT has no absorption between 450 nm and 550 nm, suggesting fair compatibility with the calcium ion imaging.

3.2. Impedance measurement

The real-time detection of cellular adhesion, proliferation, and viability are evaluated using the technique called the binary detection, which helps us determine the minimum number of recording electrodes necessary for a neuron culture of a given size. The impedance is

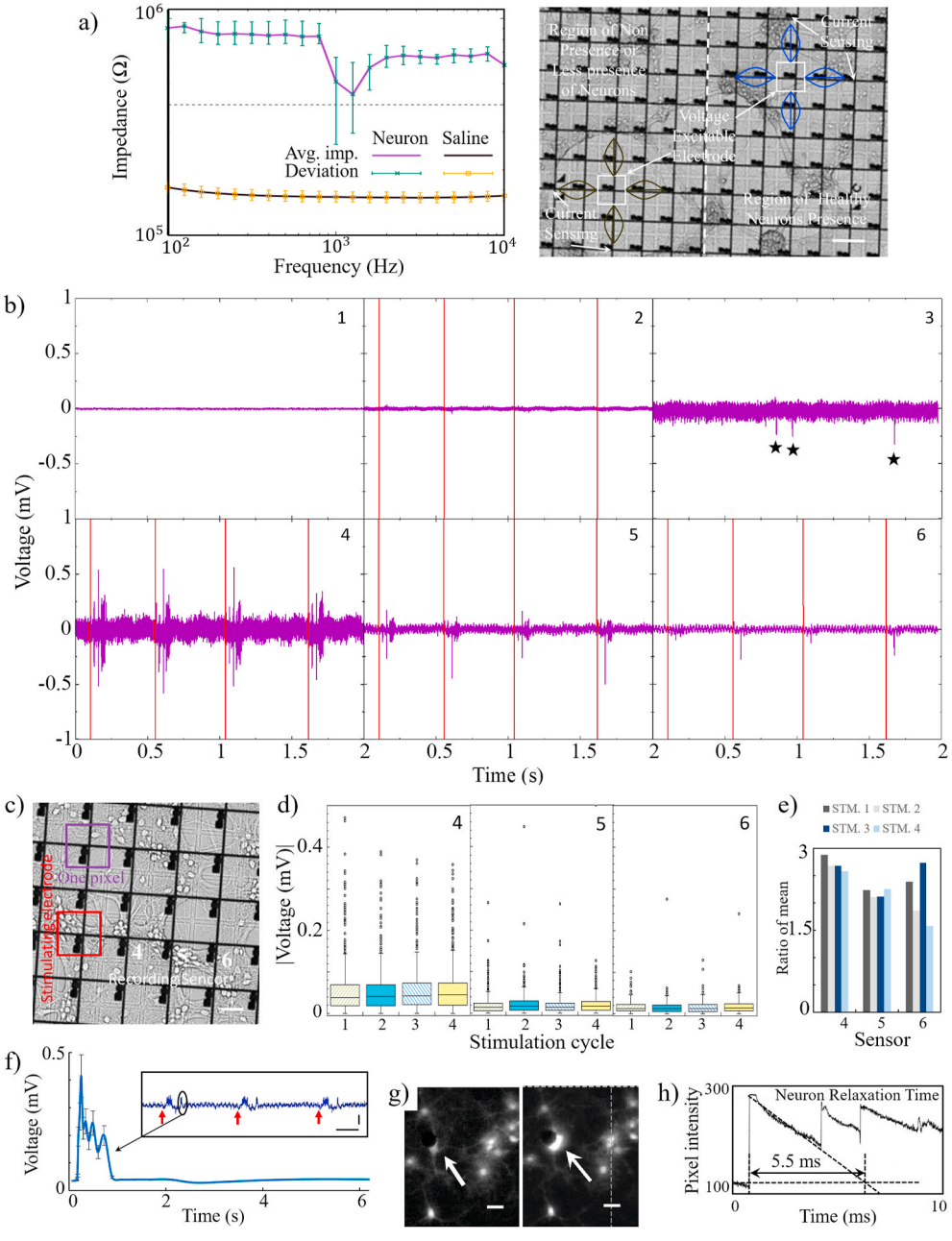

Fig. 4. Biological measurement of culture neurons: (a) (left) Impedance spectroscopy: the binary cells detection using impedance value for mapping cells presence on electrode. (right) The white rectangle represents the voltage excitable electrode. The surrounding four electrodes are used for the current reading. The blue and green line represents presence and absence of neurons. (b) Real time recorded response under study condition of, (1) only saline (relative standard deviation (RSD) is 75.4, all the calculated RSD values in this article is considering the absolute value of the data sample), (2) saline and stimulation (RSD is 71.5), (3) neuron culture atop sensor array (RSD is 72.5), (4–5) neurons response due to stimulation (RSD is 69.8, 73.66 and 65.8, respectively). (c) The recording and stimulation electrodes are shown on the neuron culture sensor chip. (d) After stimulation activity for four different stimulations are summarized for Fig. a (4–5). (e) Sensor recording repeatability: ratio of absolute mean of after and before stimulation for 25 ms interval. Sensor 4 and 5 have almost similar ratio for all the stimulations and sensor 6 responses is no constant as neurons are far from the sensor. (f) Chemical stimulation, the red arrows represent the KCl injection into the culture bath. The immediate spikes are due to KCl injection into the bath. The circled spikes (shown from first stimulation) are the response from the neuron (RSD is 126). (g) Selective single neuron stimulation with low intensity of voltage. (h) The pixel intensity of fluorescence imaging of Fig. (g). The relaxation time for the neuron is 5.5 ms. Scale bars: (a) 100 μm, (c) 50 μm, (f) 10 s and 1 mV, and (g) 50 μm. (For interpretation of the references to colour in this figure legend, the reader is referred to the Web version of this article.)

measured with and without neurons on the array immersed in a culture medium. The geometrical arrangement of electrodes for excitation and measurement is arbitrarily set by programming; for instance, they can be adjacent or separated. Electrodes can also be monitored in a selective or collective manner. The cells detection is performed either in a frequency region lower than 5 kHz or higher than 20 kHz. Normalized impedance of sub-threshold levels has been reported in a high frequency region over 10 kHz (Shaik et al., 2018). Nevertheless, low frequency measurement is preferable due to the relatively large shift in the impedance level. Typical subthreshold level of 4×10^5 Ohm is chosen in this work, as it could be used in both low and high frequency ranges.

The average impedance and the standard deviation are shown in Fig. 4(a). Comparing the impedance level with and without the neuron cells, the former is relatively high due to the capacitive component in the equivalent circuit of the live neuron cells. The standard deviation in the impedance curve for neuron is considerably higher than that in saline, primarily caused by stochastic electro-potential activities of inhomogeneous distributing cells electrode gap. It is observed that the cell death causes reduction in the impedance. The small drop-off of impedance in 8–10 kHz is due to the presence of the neural network, which equivalently acts as a band pass filter.

3.3. Biological measurement

The *in-vitro* experiments are performed to confirm the full-functionality of the chip and the measurement system. Electrical activities of cultured primary cortical neurons on the TFT chip surface are successfully measured (see Fig. 4 (b-i)). Two types of extracellular signals (LFPs and APs) are recorded and amplified by a low-noise voltage amplifier (MPA32I from Multi Channel System). The average electrical activities of neurons around the electrodes are represented as LFPs. On the other hand, electrical activities of neurons under excitation are represented by APs. The typical bandwidths for LFPs and APs are 1 Hz–300 Hz and 300 Hz −10 kHz, respectively. The stimulation capability of the device is verified by examining in different phases, such as recording from empty (no cells) TFTs, neurons on the TFTs, disconnected stimulator, and with stimulation to neurons.

The recorded neurons activities mapped at the corresponding sensor positions are shown in Fig. 4(b). The signals in frames 1 and 2 in Fig. 4 (b) are obtained under conditions without neurons culture but with a stimulator disconnected and connected, respectively, while the signal in frame 3 is obtained from the cultured neurons without stimulations. The spikes with a star mark (★) represent the spontaneous activities of the neurons. The signals in frames 4 and 5 are from the culture neurons shown in Fig. 4(c) that experienced stimulations. The stimulation pulses are shown in the red vertical lines. The intensity and amplitude of the neuron spikes vary from electrode to electrode due to several reasons, such as electrical coupling between the neurons and the electrode, mutual distance from the recorded electrodes, and density of the neurons around the site of stimulations.

Distribution of recorded signal after each stimulation is shown in Fig. 4(d), where minimum, first quartile, median, third quartile and maximum are plotted. The propagation loss is seen in Fig. 4(d). The repeatability of measurement is confirmed by the mean ratio of signals 25 ms before and after the stimulation, as shown in Fig. 4(e) for sensors 4 and 5; the fluctuation in sensor 6 is due to the unstable environmental conditions, with the neurons sitting far from the sensor. With a low intensity of stimulation, single neuron can be targeted as shown in Fig. 4 (g), wherein the pixel intensity of the florescence activity of the neuron is monitored as shown in Fig. 4(h). The relaxation time for each stimulation is estimated to be 5.5 ± 1 ms.

In addition to the electrical stimulation, chemical stimulation has also been carried out using potassium chloride (KCl). K^+ ions concentration level is usually high inside the cell (~150 mM) compared with the outside (~3 mM), which allows K^+ ions to transport to the extracellular environment via the leaking channels, causing hyperpolarization of the cell membrane. Injection of a KCl solution from a pipette causes increase of K^+ ions in the extracellular environment, which blocks the outward movement of positively charged K^+. As a result, K^+ remaining in the cytoplasm leaves the membrane depolarized as shown in Fig. 4(f).

The activities of two clusters of neurons shown in **Fig. 5(a)** are recorded as plotted in Fig. 5(c); measurement is repeated by manually switching the gate lines for pre-programed stimulation signals**.** Intensity of recorded signal decline with increasing distance and vice versa. The efficiency of sensor with respect to distance is shown in Fig. 5(b). The minimum and maximum delay between stimulation and spikes observed are 6.5 ms and 14.5 ms, respectively, as shown in Fig. 5(d). Signals from two electrodes are monitored for more than an hour and superposed as shown in Fig. 5(e). The recoded raw data are further processed to calculate firing rate and delay time. The average stimulus-firing rate is approximately 15–17 spikes/s, whereas the maximum is 27 spikes/s, as shown in Fig. 5(f). The spontaneous activity of neurons is about 4 spikes/s as shown in Fig. 5(g).

4. Comparison with the state-of-the-art

The performance of the developed TFT chip has been summarized and compared with other states-of-the-art devices used for electrogenic cells study as shown in Table 1. In the past, a large number of studies have been carried out on opaque substrates such as silicon-based MOSFET and ion-sensitive field-effect transistor. A trade-off exists in the conventional MEAs between the substrate transparency and the electrode density; achieving the high transparency required a sparse electrode density and vice-versa. However, the advantage of the TFT solution is that it has a high transparency without compromising the electrode density. A 32-channel recording system with addressable electrodes has been developed in this work to successfully detect the change of the electrical impedance caused by the presence of neurons on the substrate. Theoretically, it is possible to perform real-time cell monitoring using the impedance characterization. The optical transmissivity is advantageous for visual monitoring of cells.

ITO is used in this work as a transparent conductor because of the superior electrical property and the matured fabrication processes. However, ITO is also known to have lattice mismatch with other materials, stress-strain constraints, and degradation due to mechanical stresses, which may restrict the potential use. Recent years, carbon nanotubes have drawn escalating attention for their superior material properties such as high elastic modulus (~1–2 TPa), high electrical conductivity, and high tensile strength (~13–53 GPa) (Hong and Myung, 2007). Carbon nanotubes have been used as a transparent electrode material for neural network study (Cellot et al., 2017; Gulino et al., 2019).

5. Conclusion

An arrayed biosensor chip with six modalities for neuronal ensemble investigation has been developed using the thin-film-transistor (TFT) technology, and characterized from electrophysiological, electrochemical and optical points of view. The electrodes are designed in such a way that they can accommodate all the necessary features as an ideal readout system to understand the complex neuronal behaviors. Besides CMOS, the high definition TFT system includes the largest number of measurement or stimulation functions to date, consisting of optical observation, impedance measurement, voltage recording as well as electrical and chemical stimulation capabilities. At the same time, it features the largest electrode fill factor (97.5%) and high transparency (>90%) over a large sensor area (243 mm^2). The temporal resolution (10 ms), spatial resolution (50 μm or 100 μm), signal to noise ratio (80 dB), and stability (over 1 billion pulses) are also comparable to those of the state-of-the-art systems. Biological studies demonstrate that the TFT biosensor chip can record neuronal activity with high fidelity as

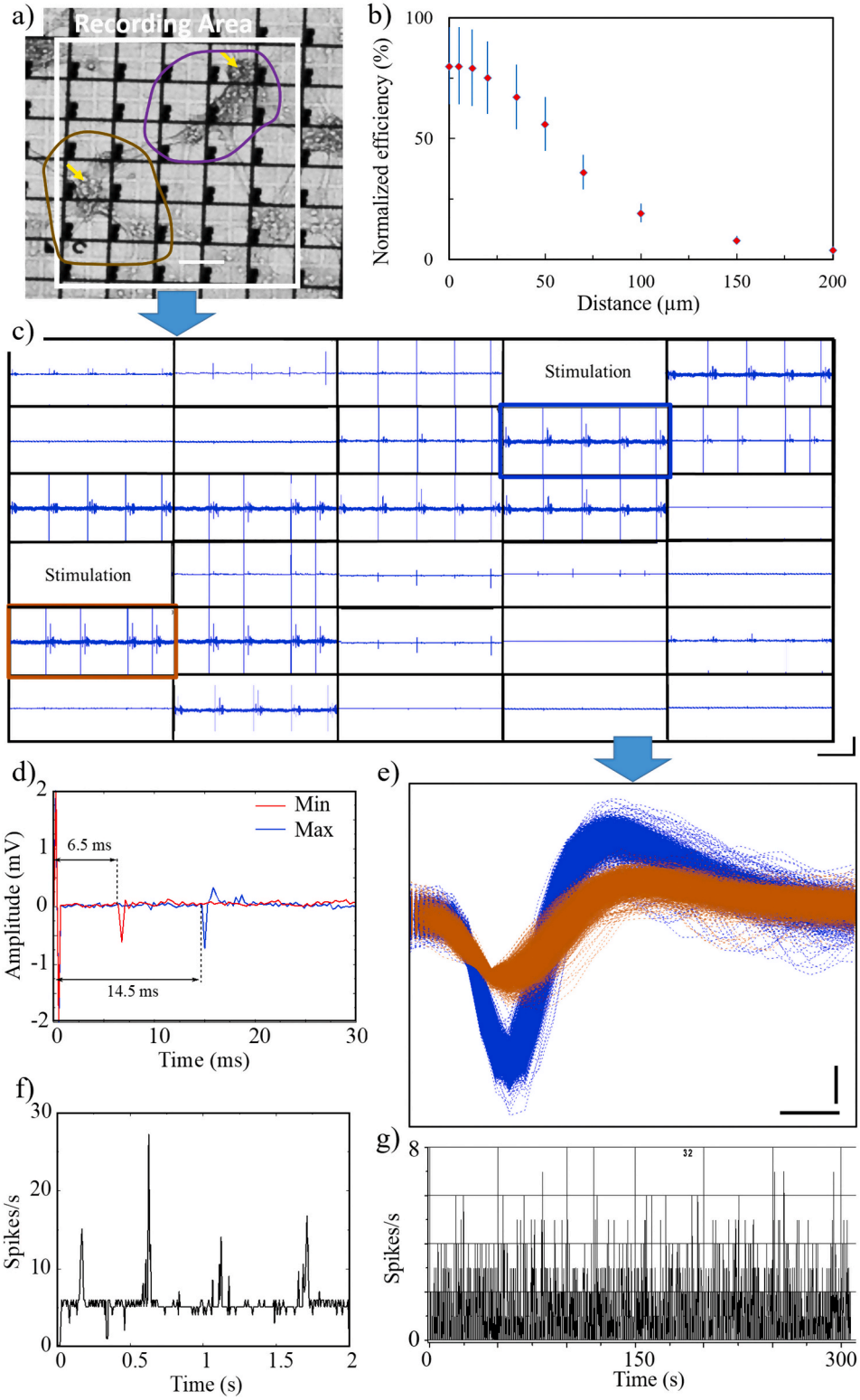

Fig. 5. Recording and signal analysis: (a) Identifying the recording electrode by utilizing the impedance spectroscopy, which target two clusters of neurons. (b) Normalized sensing efficiency of a sensor with respect to distance between the neuron and the sensor. (c) Recorded Signal from the 5 × 6 sites reconstructed after several 1D measurements. (d) Latency time (e) Spikes from two different clusters. (f) Spike rate due to stimulation. (g) Spontaneous spike rate. Scale bar: (a) 100 μm, (c) 0.5 s and 1 mV, and (e) 0.1 ms and 50 μV.

conventional MEAs, while the noise level has room for improvement. The test chip with a 4-μm-wide gate is incapable of on-chip current stimulation. Nevertheless, the electrical measurements indicate that the larger transistor size (>17 μm) is helpful for on-chip current stimulation with affordable penalty of losing the overall optical transparency. Increasing the drain voltage, which may cause cell's death due to overheating, can reduce the transistor gate width. Thus, further investigation is needed to solve the tradeoff between transistor gate width and the voltage. Based on the experimental results, the multimodal operation has been found feasible. In order to control different operations, a control system is under development. The TFT chip is exploring the quest for versatile characterization of biological sample. All these features will pave the way of whole TFT system towards complex experiment that can target multiple cellular parameters at

Table 1
Performance summary and comparison of *in-vitro* systems.

Reference	Song et al. (2012)	Chi et al. (2015)	Dragas et al. (2017)	Benfenati et al. (2013)	This Work
Technology	MEA	CMOS	CMOS	Organic Cell Stimulating and Sensor Transistor	**TFT**
Pixel Type	Passive	Active	Switch Matrix	Active	**Active Switch Matrix**
Total Active Area	0.18 mm^2	~1 mm^2 (9-pixel group)	~10 mm^2	~1 mm^2	**243 mm^2**
No. of Electrodes	64	144	59,760	1	**30,000**
Electrode Pitch	30 μm	40 μm	13.5 μm	30 μm × 15 mm channel	**50 or 100 μm**
Electrode Gap	100 μm	60 μm	-	-	**2.5 or 5 μm**
No. Different Measurement Modes	2	4	5	2	**6**
Electrode density	4.1%	20%	12.34%	-	**97.5%**
Maximum amplitude to noise ratio	4	5	12	22	**17**
Sampling Rate	25 kS/s	-	20 kS/s	-	**25 kS/s**
Transparency	-	Opaque	Opaque	Only the channel	**95%**
Thermal noise	-	-	8 × 10^{-20} W	-	**8 × 10^{-20} W**
Addressable electrodes with N address lines	N	$(N/2)^2$	$(N/2)^2$	N	**$(N/2)^2$**
Stimulation	V	-	V or I	V	**V or I**
Die Size	76.2 mm × 25.5 mm	2.2 mm × 2 mm	12 mm × 8.9 mm	-	**25 mm × 27 mm**

once.

CRediT authorship contribution statement

Faruk Azam Shaik: Writing- original draft. **Hiroshi Toshiyoshi:** Writing - review & editing.

Declaration of competing interest

The authors declare that they have no known competing financial interests or personal relationships that could have appeared to influence the work reported in this paper.

Acknowledgement

This work was supported by JSPS Grant-in-Aid for Scientific Research (B) Grant Number 15H03984.

References

Abdelfattah, A.S., Farhi, S.L., Zhao, Y., Brinks, D., Zou, P., Ruangkittisakul, A., Platisa, J., Pieribone, V.A., Ballanyi, K., Cohen, A.E., Campbell, R.E., 2016. J. Neurosci. 36, 2458–2472.
Angle, M.R., Cui, B., Melosh, N.A., 2015. Curr. Opin. Neurobiol. 32, 132–140.
Azim, N., Hart, C., Sommerhage, F., Aubin, M., Hickman, J.J., Rajaraman, S., 2019. J. Microelectromechanical Syst. 28, 50–62.
Aziz, J.N.Y., Abdelhalim, K., Shulyzki, R., Genov, R., Bardakjian, B.L., Derchansky, M., Serletis, D., Carlen, P.L., 2009. IEEE J. Solid State Circ. 44, 995–1005.
Benfenati, V., Toffanin, S., Bonetti, S., Turatti, G., Pistone, A., Chiappalone, M., Sagnella, A., Stefani, A., Generali, G., Ruani, G., Saguatti, D., Zamboni, R., Muccini, M., 2013. Nat. Mater. 12, 672–680.
Bertotti, G., Velychko, D., Dodel, N., Keil, S., Wolansky, D., Tillak, B., Schreiter, M., Grall, A., Jesinger, P., Rohler, S., Eickenscheidt, M., Stett, A., Moller, A., Boven, K.H., Zeck, G., Thewes, R., 2014. In: IEEE 2014 Biomedical Circuits and Systems Conference, BioCAS 2014 - Proceedings, pp. 304–307.
Brewer, G.J., Torricelli, J.R., Evege, E.K., Price, P.J., 1993. J. Neurosci. Res. 35, 567–576.
Brody, T.P., Asars, J.A., Dixon, G.D., 1973. IEEE Trans. Electron. Dev. 20, 995–1001.
Cabello, M., Aracil, C., Perdigones, F., Mozo, M., de la Cerda, B., Quero, J.M., 2018. Sensor. Actuator. B Chem. 257, 954–962.
Cathcart, G.A., Tixier-Mita, A., Ihida, S., Eiler, A.-C., Toshiyoshi, H., 2020. IEEJ Trans. Sensors Micromachines 140, 193–200.
Cathcart, G.A., TIxier-Mita, A., Ihida, S., Shaik, F., Toshiyosh, H., 2017. In: TRANSDUCERS 2017 - 19th International Conference on Solid-State Sensors. Actuators and Microsystems, pp. 1672–1675.
Cathcart, G.A., Tixier-Mita, A., Ihida, S., Shaik, F.A., Toshiyoshi, H., 2016. In: 2016 IEEE 11th Annual International Conference on Nano/Micro Engineered and Molecular Systems, NEMS 2016, pp. 379–383.
Cellot, G., La Monica, S., Scaini, D., Rauti, R., Bosi, S., Prato, M., Gandolfi, S., Ballerini, L., 2017. J. Biomed. Nanotechnol. 13, 559–565.
Chi, T., Park, J.S., Butts, J.C., Hookway, T.A., Su, A., Zhu, C., Styczynski, M.P., McDevitt, T.C., Wang, H., 2015. IEEE Trans. Biomed. Circuits Syst. 9, 801–814.
Chu, C.H., Sarangadharan, I., Regmi, A., Chen, Y.W., Hsu, C.P., Chang, W.H., Lee, G.Y., Chyi, J.I., Chen, C.C., Shiesh, S.C., Lee, G. Bin, Wang, Y.L., 2017. Sci. Rep. 7, 1–15.
Cohen-Karni, T., Qing, Q., Li, Q., Fang, Y., Lieber, C.M., 2010. Nano Lett. 10, 1098–1102.
Correia, A.P.P., Barquinha, C., Goes, P.M., Palma, J.C. da, 2016. In: A Second-Order ΣΔ ADC Using Sputtered IGZO TFTs, pp. 3–8.
Dietzel, A., 2016. Microsystems for Pharmatechnology. Springer, Cham.
Dragas, J., Viswam, V., Shadmani, A., Chen, Y., Bounik, R., Stettler, A., Radivojevic, M., Geissler, S., Obien, M.E.J., Müller, J., Hierlemann, A., 2017. IEEE J. Solid State Circ. 56, 1576–1590.
Dunnett, S.B., Björklund, A., 1997. Brain Res. Protoc. 1, 91–99.
Foidl, B.M., Ucar, B., Schwarz, A., Rebelo, A.L., Pandit, A., Humpel, C., 2018. J. Neurosci. Methods 295, 77–86.
Franke, K., Berens, P., Schubert, T., Bethge, M., Euler, T., Baden, T., 2017. Nature 542, 439–444.
Grienberger, C., Konnerth, A., 2012. Neuron 73, 862–885.
Grskovic, M., Javaherian, A., Strulovici, B., Daley, G.Q., 2011. Nat. Rev. Drug Discov. 10, 915–929.
Gulino, M., Kim, D., Pané, S., Santos, S.D., Pêgo, A.P., 2019. Front. Neurosci. 13, 689.
Harris, K.M., 2018. Some typical dimensions of dendrites for a few types of neurons. SynapseWeb [WWW Document]. URL. https://synapseweb.clm.utexas.edu/dimensions-dendrites. accessed 15.8.2020.
Heer, F., Hafizovic, S., Franks, W., Blau, A., Ziegler, C., Hierlemann, A., 2006. IEEE J. Solid State Circ. 41, 1620–1629.
Hess, L.H., Jansen, M., Maybeck, V., Hauf, M.V., Seifert, M., Stutzmann, M., Sharp, I.D., Offenhäusser, A., Garrido, J.A., 2011. Adv. Mater. 23, 5045–5049.
Hong, S., Myung, S., 2007. Nat. Nanotechnol. 2, 207–208.
Hood, S.J., Kampouris, D.K., Kadara, R.O., Jenkinson, N., Del Campo, F.J., Muñoz, F.X., Banks, C.E., 2009. Analyst 134, 2301–2305.
Kim, Y.H., Kim, G.H., Kim, A.Y., Han, Y.H., Chung, M.A., Jung, S.D., 2015. J. Neural. Eng. 12, 066029.
Kojiri, T., Matsuda, T., Kimura, M., 2014. Jpn. J. Appl. Phys. 53, 125802.
Le Comber, P.G., Spear, W.E., Ghaith, A., 1979. Electron. Lett. 15, 179–181.
Lee, J., Ozden, I., Song, Y.K., Nurmikko, A.V., 2015. Nat. Methods 12, 1157–1162.
Leppert, W., Zajaczkowska, R., Wordliczek, J., Dobrogowski, J., Woron, J., Krzakowski, M., 2016. J. Physiol. Pharmacol. 67, 787–799.
Lu, C., Chen, Q., Zhou, T., Bozic, D., Fu, Z., Pan, J.Q., Feng, G., 2016. Mol. Psychiatr. 21, 159–168.
Matsuda, T., Umeda, K., Kato, Y., Nishimoto, D., Furuta, M., Kimura, M., 2017. Sci. Rep. 7, 44326.
Müller, J., Ballini, M., Livi, P., Chen, Y., Radivojevic, M., Shadmani, A., Viswam, V., Jones, I.L., Fiscella, M., Diggelmann, R., Stettler, A., Frey, U., Bakkum, D.J., Hierlemann, A., 2015. Lab Chip 15, 2767–2780.
Nomura, K., Ohta, H., Takagi, A., Kamiya, T., Hirano, M., Hosono, H., 2004. Nature 432, 488–492.
Nomura, K., Ohta, H., Ueda, K., Kamiya, T., Hirano, M., Hosono, H., 2003. Science 80, 1269–1272, 300.
Park, J., Lee, B.K., Jeong, G.S., Hyun, J.K., Lee, C.J., Lee, S.H., 2015. Lab Chip 15, 141–150.
Park, J.S., Aziz, M.K., Li, S., Chi, T., Grijalva, S.I., Sung, J.H., Cho, H.C., Wang, H., 2018. IEEE Trans. Biomed. Circuits Syst. 12, 80–94.
Park, J.W., Vahidi, B., Taylor, A.M., Rhee, S.W., Jeon, N.L., 2006. Nat. Protoc. 1, 2128.
Pottosin, I., Dobrovinskaya, O., 2015. Front. Physiol. 6, 396.
Ruther, P., Paul, O., 2015. Curr. Opin. Neurobiol. 32, 31–37.
Santoro, F., Dasgupta, S., Schnitker, J., Auth, T., Neumann, E., Panaitov, G., Gompper, G., Offenhäusser, A., 2014. ACS Nano 8, 6713–6723.
Shaik, F.A., Cathcart, G.A., Ihida, S., Ikeuchi, Y., Tixier-Mita, A., Toshiyoshi, H., 2018. J. Microelectromechanical Syst. 27, 423–433.
Shaik, F.A., Ihida, S., Tixier-Mita, A., Toshiyoshi, H., 2020. In: Santra, T.S., Tseng, F.-G. (Eds.), Handbook of Single Cell Technologies. Springer Singapore, pp. 1–27.
Shaik, F.A., Ikeuchi, Y., Cathcart, G., Ihida, S., Toshiyoshi, H., TIxier-Mita, A., 2017. In: TRANSDUCERS 2017 - 19th International Conference on Solid-State Sensors. Actuators and Microsystems, pp. 206–209.

Shen, W., Karumbaiah, L., Liu, X., Saxena, T., Chen, S., Patkar, R., Bellamkonda, R.V., Allen, M.G., 2015. Microsystems Nanoeng 1, 1–2.
Snell, A.J., Mackenzie, K.D., Spear, W.E., LeComber, P.G., Hughes, A.J., 1981. Appl. Phys. 24, 357–362.
Song, Y., Lin, N., Liu, C., Jiang, H., Xing, G., Cai, X., 2012. Biosens. Bioelectron. 38, 416–420.
Spear, W.E., Le Comber, P.G., 1993. Solid State Commun. 88, 1015–1018.
Spira, M.E., Hai, A., 2013. Nat. Nanotechnol. 8, 83–94.
Weimer, P.K., 1962. Proc. IRE 60, 1462–1469.
Wikswo, J.P., Block, F.E., Cliffel, D.E., Goodwin, C.R., Marasco, C.C., Markov, D.A., McLean, D.L., McLean, J.A., McKenzie, J.R., Reiserer, R.S., Samson, P.C., Schaffer, D. K., Seale, K.T., Sherrod, S.D., 2013. IEEE Trans. Biomed. Eng. 60, 682–690.
Yamamoto, Y., 2012. Jpn. J. Appl. Phys. 51, 060001.
Zanos, T.P., Mineault, P.J., Pack, C.C., 2011. J. Neurophysiol. 105, 474–486.